

# A Tri-port DC-DC Converter for Bifacial PV Panels Coupled with Energy Storage

Research paper

Preeti Kumari Sahu<sup>1,\*</sup>, Karpana Sivakrishna<sup>1</sup>, Efstratios I. Batzelis<sup>2</sup>,  
Chandan Chakraborty<sup>1</sup>, J. N. Roy<sup>1</sup>

<sup>1</sup>Indian Institute of Technology Kharagpur, Kharagpur, India

<sup>2</sup>University of Southampton, Southampton, UK

Received: 22 March 2024; Accepted: 05 July 2024

**Abstract:** The power output of photovoltaic (PV) systems, especially bifacial modules, varies due to daily fluctuations in irradiance and temperature. Maximising the efficiency and power extraction are considered crucial. Hybrid DC off-grid topologies are highly promising for rural electrification with solar energy and battery backup. These systems, tailored for household appliance use, feature low semiconductor count, continuous current ports for PV, battery and DC loads, low-voltage levels for PV and battery, voltage regulation for DC loads, maximum power point tracking (MPPT), proper battery charging and discharging, high-voltage boosting without low-frequency transformers and reduced power converter stages. However, the existing schemes often lack the above-mentioned critical features. Hence, this paper proposes a novel three-switch tri-port converter with integrated energy storage for stand-alone bifacial PV applications, with modelling and experimental validation. The battery serves as an energy storage component, regulating the DC link voltage for consistency. This paper underscores PV system power optimisation and introduces a novel tri-port converter for stand-alone bifacial PV setups, emphasising energy storage's role in voltage regulation.

**Keywords:** 5-parameter electrical model • bifacial PV system • DC bus voltage regulation introduction • energy storage element • I-V curve

## 1. Introduction

Renewable energy is indeed a sustainable and clean power source, harnessing natural resources such as sunlight, wind and water to generate electricity. This reduces reliance on fossil fuels and helps mitigate the associated environmental impacts (IEA, 2021). Among renewable energy technologies, bifacial photovoltaic (PV) systems stand out for their innovative approach. Unlike traditional solar panels that utilise only their front side, bifacial PV technology uses both the front and rear sides to capture sunlight (de Melo et al., 2022). Bifacial PV systems can significantly boost energy generation by harnessing reflected and scattered light from surrounding surfaces, resulting in higher efficiency and increased design flexibility (Sahu et al., 2023a). This technology is particularly beneficial for residential applications, where the good reflectivity from white-painted roofs enhances performance.

Bifacial PV generation exhibits fluctuations throughout the day and disappears at night, rendering it unsuitable as a constant energy source for essential loads or the grid (Li and Wolfs, 2008; Selvaraj and Rahim, 2008). Nonetheless, a PV/battery (PV/Bat) hybrid energy system can address the intermittent nature of solar energy and deliver continuous power. Conventionally, this necessitates the use of two DC-DC converters or a tri-port converter to connect the PV array, the battery and the load. This combination helps improve the overall system's reliability (Bird et al., 2013).

The traditional PV/Bat hybrid system typically involves the use of two separate converters. One converter is dedicated to converting PV energy, whereas the other is responsible for charging or discharging the battery. This setup, although effective, reduces the power density of the system because of the more than one converter

\* Email: preeti.eee20@gmail.com

requirement. Alternatively, these two individual converters can be substituted by a three-port converter (TPC) to enhance the power density. The main benefit of TPCs lies in the sharing of their components during states and different operation modes (Bhattacharjee et al., 2018). There is extended literature available dealing with multiport topologies. For instance, some reported topologies necessitate at least six switches (Wang and Li 2012), whereas others require only three switches and three diodes (Li et al., 2011; Mohammadi et al., 2022). Despite their potential, the high demand for inductors, capacitors, semiconductor switches and associated driver circuits and power supplies limits their practicality. Moreover, none of the reported topologies have been validated for bifacial PV stand-alone applications.

To fully utilise the power-generation capacity of solar energy sources, a maximum power point tracking (MPPT) controller is also necessary (Manuel and İnanç 2022). However, maximising the energy output of bifacial PV systems poses unique challenges, particularly in the presence of self-shading. Shading can significantly impact the performance of the front and rear sides of bifacial modules, rendering traditional MPPT algorithms less effective (Raina et al., 2022). This necessitates the development of MPPT techniques explicitly tailored for bifacial PV systems. A comprehensive literature survey reveals that several studies have been conducted on MPPT techniques for bifacial PV systems (Perera and Wen, 2019; Phimu et al., 2021; Siddiqui et al., 2022, 2023). Researchers have explored various approaches, including advanced algorithms based on artificial intelligence, machine learning and fuzzy logic. These studies have highlighted the importance of considering shading effects on the bifacial modules' front and rear sides during the MPPT process. The research findings suggest that modified MPPT algorithms can significantly improve the energy-harvesting efficiency of bifacial PV systems under self-shading conditions. However, further research is needed to optimise and validate these techniques to ensure their practical applicability and effectiveness. One such algorithm for bifacial PV is proposed in Sahu et al. (2023b). In this paper, the proposed algorithm is utilised to locate the Maximum Power Point (MPP) voltage from bifacial PV.

To address the aforementioned concerns, this paper presents a tri-port converter topology for integrating bifacial PV modules with battery to regulate the DC link voltage. The proposed TPC stands out for its effective solutions to several key concerns, highlighted by the following features:

- (a) Addressing self-shading issues: It incorporates the proposed algorithm for the calculation of the MPP voltage for the bifacial PV, providing a solution for the self-shading problem;
- (b) Integrated energy storage: It ensures a stable DC link voltage despite PV/load fluctuations and caters to nighttime load demands; and
- (c) Single power inductor multiport approach: This innovative approach uses a single power inductor to manage multiple ports, streamlining the system and potentially reducing cost and complexity.

This paper begins by discussing the characteristics of bifacial PV modules and the algorithm for estimating the MPP voltage in Section II. Section III provides a brief introduction to the proposed TPC converter, explaining how it efficiently regulates and manages power flow between the bifacial PV module and the battery. The design and modelling of the proposed system are discussed in detail in Section IV. The experimental results, validating the TPC system's real-world performance, are presented in Section VI. A study on the performance stability and reliability of the system is showcased in Section VII. Section VIII compares the proposed topology with the existing tri-port topologies. Finally, Section VIII delves into loss analysis and efficiency calculation followed by the concluding remark in Section IX.

## 2. Characteristics of Bifacial PV Modules

### 2.1. Bifacial PV electrical circuit model

The bifacial PV model utilises a single-diode circuit (Zhen et al., 2021), where each bifacial parameter is dependent on the corresponding front and rear parameters. The circuit diagram of the model is depicted in Figure 1, whereas the equations representing the model are provided in Sahu et al. (2023b).

To convert the five reference parameters ( $I_{phB}, I_{sB}, a_B, R_{sB}, R_{shB}$ ) at operating conditions ( $G_0$  and  $T_0$ ) to their corresponding values ( $I_{ph}, I_s, a, R_s, R_{sh}$ ) at the actual operating condition ( $G$  and  $T$ ), the translation equations proposed by Batzeliis (2017) are utilised.

## 2.2. Rear side shading

Shading can significantly impact the energy output of bifacial PV systems, as shading on one side of the panel can affect the energy output of both sides. Here are a few shading scenarios that are important to consider for bifacial PV systems:

- (a) Self-shading: Self-shading occurs when the PV panel casts a shadow on itself, which can reduce the energy output of both sides of the panel. Self-shading can occur when the spacing between the panels is too narrow or when the panels are tilted at an angle that causes shadows to be cast on adjacent panels.
- (b) Ground shading: Ground shading occurs when shadows are cast on the underside of the bifacial PV panel, which can reduce the panel's energy output. Ground shading can be caused by objects such as trees, buildings or nearby structures that cast shadows on the ground.
- (c) Backside shading: Backside shading occurs when shadows are cast on the backside of the bifacial PV panel, which can reduce the energy output of the panel. Backside shading can be caused by nearby structures or objects that cast shadows on the panel's backside.
- (d) Edge shading: Edge shading occurs when shadows are cast on the edges of the bifacial PV panel, which can reduce the panel's energy output. Edge shading can be caused by objects such as trees, buildings or nearby structures that cast shadows on the edges of the panel.

The impact of shading scenarios must be carefully considered to maximise the energy output of bifacial PV systems. In one specific example depicted in Figure 2, the shading on the rear side of the bifacial module affects the overall I–V curve. Therefore, an algorithm is needed to estimate the maximum power of the module's front

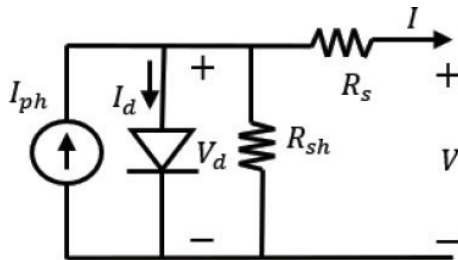
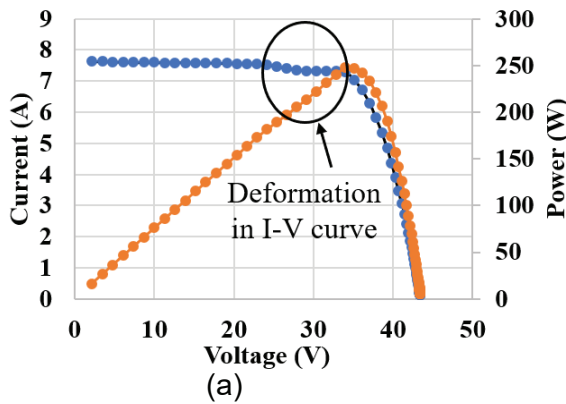


Figure 1. Single-diode electrical equivalent circuit of the bifacial PV cell. PV, photovoltaic.



Parameters	Measured Value	Predicted Value
$P_m$	247.8	253.6
$V_m$	34.7	34.9
$I_m$	7.14	7.26
$V_{oc}$	43.5	43.9
$I_{sc}$	7.6	7.6

(b)

Figure 2. One instance of the I–V curve at self-shading (a) deformation in the I–V curve and (b) comparison between measured and predicted values.

and rear sides individually. This study utilises the MPP voltage,  $V_m$ , estimation algorithm proposed by Sahu et al. (2023b), which provides a comprehensive explanation of this algorithm, outlining how it accurately estimates the maximum power of the bifacial PV system by considering the front and rear sides power contributions separately and combining them effectively. This approach ensures that the impact of self-shading on the rear side is not overlooked.

### 3. Proposed PV/Bat Tri-port DC-DC Converter (PV/Bat TPC)

The proposed TPC hybrid system is shown in Figure 3, featuring a series connection of all three input ports and their respective sources. The converter configuration consists of two inductors denoted as  $L$  and  $L_{filter}$  and three semiconductor switches denoted as  $S_{bp}$ ,  $S_{pv}$  and  $S_{bat}$  with a battery port eventually linked to the DC link port. This configuration effectively addressed several critical challenges commonly encountered in PV systems.

In the classical hybrid PV/Bat structure, two power inductors are used, which reduces the power density of the converter. However, the proposed converter utilises a single power inductor, which optimises the magnetic size and increases the power density. Additionally, in the classical converter, the voltage stress on all the switches and diodes is the same as the DC link voltage. In contrast, in the proposed converter, only one switch ( $S_{pv}$ ) has a high voltage rating, which is the sum of the DC link voltage and the battery voltage. All other switches ( $S_{bp}$  and  $S_{bat}$ ) carry a low voltage, either the battery voltage or the PV voltage. As a result, switching losses are reduced because the  $R_{ds(on)}$  is lower.

Details of the essential gate pulse sequence for the switches can be observed in Figure 4. The proposed TPC can be operated in six distinct operational modes, as depicted in Table 1. The determination of these modes is influenced by various factors, including varying illumination levels among individual PV sub-strings, connected loads, battery status and the time of day. A detailed overview of these modes along with a comprehensive understanding of the average switch current status during various switching states for both charging and discharging instances of the battery is given in Figure 4.

The charging and discharging duties are denoted as  $d_{ch}^{eff}$  and  $d_{dis}^{eff}$ , respectively. During the discharging period,  $d_{dis} \leq d_{pv}$ , and during the charging period,  $d_{ch} \leq d_{pv}$ . This implies that the charging of the battery is limited to  $d_{pv}$ , and

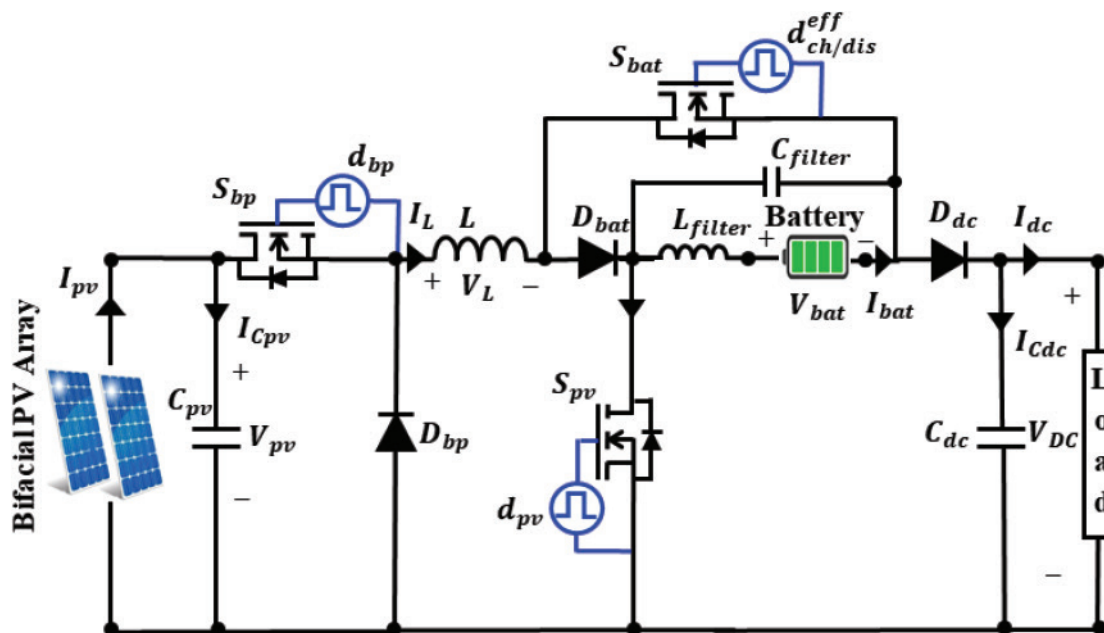


Figure 3. Proposed bifacial PV/Bat Tri-port DC-DC converter.

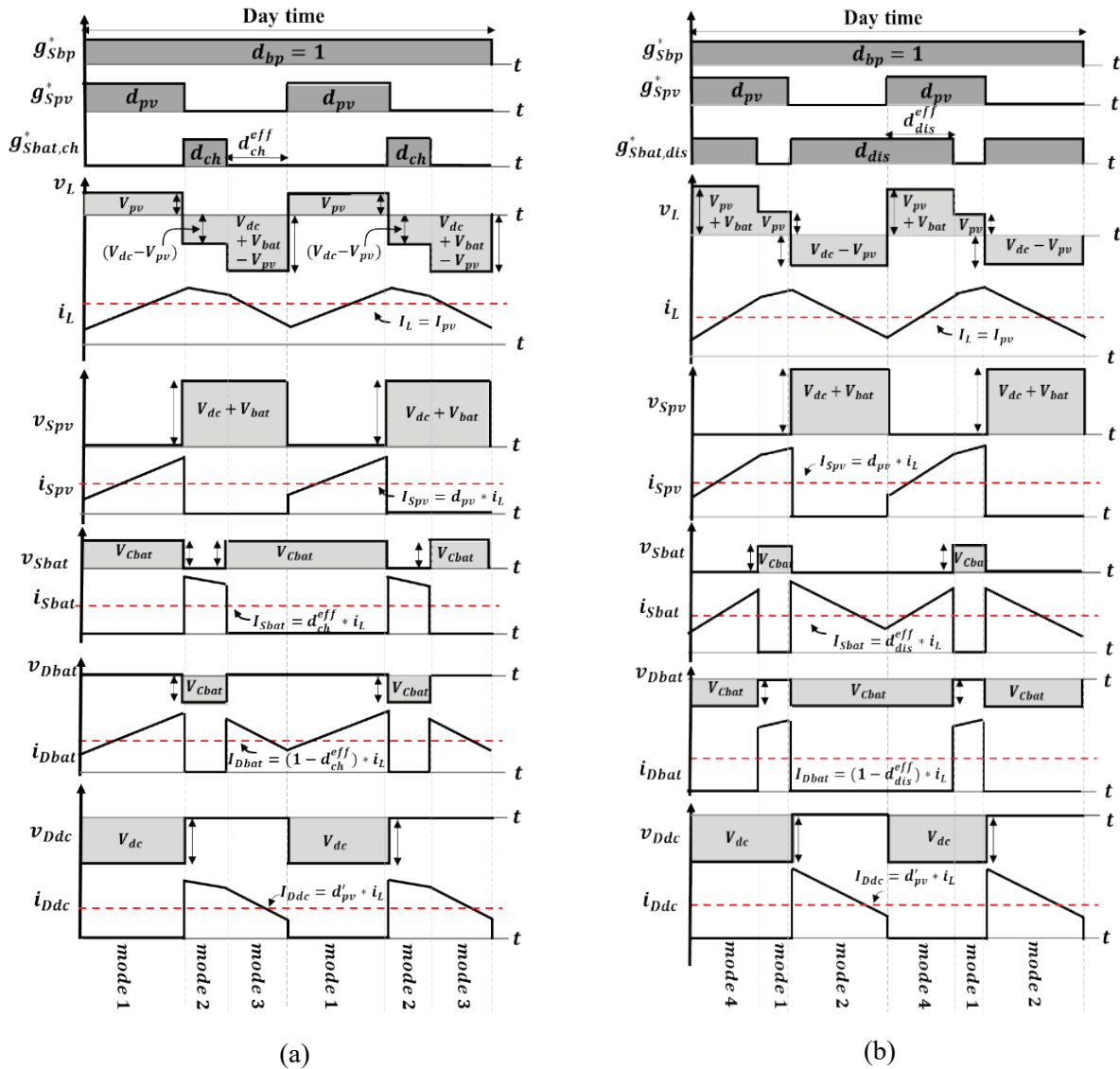


Figure 4. Voltage and current profile of the inductor and switches for battery (a) charging (daytime) and (b) discharging (daytime).

the discharging of the battery is restricted to  $d_{pv}$ . These limitations ensure that the battery operation remains within the specified boundaries and is effectively managed, optimising the overall performance of the system.

### 4. Design and Modelling of the Proposed Bifacial PV/Bat TPC

In this scenario, data from an existing rooftop-based 6 kW<sub>p</sub> bifacial PV system, specifically the Adani ASB-7-380 (PERC Bifacial, 2021), have been utilised. These data are employed for sizing and configuring the system, with consideration given to specific load profiles during the daytime and nighttime operations on a summer day (Vračar and Pejović, 2022). A detailed breakdown of this information is provided in Table 2.

#### 4.1. Sizing of the system

In this configuration, the 6 kW<sub>p</sub> PV capacity is divided into four strings, with each string comprising four PV modules connected in series. As a result, the PV system’s specifications are: 6 kW<sub>p</sub>, 160 V, and 38.4 A at STC (standard

**Table 1.** Switching status of different modes.

Modes	Switching status	Remark
Mode 1	$S_{bp}$ : ON, $S_{pv}$ : ON, $S_{bat}$ : OFF	Daytime operation, PV charges inductor, battery is idle.
Mode 2	$S_{bp}$ : ON, $S_{pv}$ : OFF, $S_{bat}$ : ON	Daytime operation, inductor discharges to the DC link.
Mode 3	$S_{bp}$ : ON, $S_{pv}$ : OFF, $S_{bat}$ : OFF	Daytime operation, inductor discharges to battery and DC link, battery is charging.
Mode 4	$S_{bp}$ : ON, $S_{pv}$ : ON, $S_{bat}$ : ON	Daytime operation, PV and battery charges inductor, and battery is discharging.
Mode 5	$S_{bp}$ : OFF, $S_{pv}$ : ON, $S_{bat}$ : ON	Nighttime operation, battery is discharging.
Mode 6	$S_{bp}$ : OFF, $S_{pv}$ : OFF, $S_{bat}$ : ON	Nighttime operation, inductor is discharging.

PV, photovoltaic.

**Table 2.** Load profile for sizing the bifacial PV/Bat.

Parameters	Ratings
Load and irradiance profile	Daytime energy need ( $Wh_{day}$ ): 20 kWh Nighttime energy need ( $Wh_{night}$ ): 6.5 kWh Total energy need ( $Wh_{tot}$ ): 26.5 kWh Average load power (day-time) ( $P_{avg,day}$ ): 4 kW Average load power (night-time) ( $P_{avg,night}$ ): 1.3 kW Peak load power ( $P_{peak}$ ): 4.1 kW Sun hours a day (at 1 kW/m <sup>2</sup> ) ( $H_{at,mp}$ ): 5h.
Sizing of the battery	Efficiency of the battery ( $E_{bat}$ ): 80% Depth of discharge of the battery (DOD): 80% Required storage capacity ( $Wh_{storage}$ ): $\frac{Wh_{night}}{E_{bat}} = 8.125$ kWh Required battery capacity ( $Wh_{bat}$ ): $\frac{Wh_{storage}}{DOD} = 10$ kWh Selected battery unit: 12 V, 26 Ah (Lead-acid), Total battery pack: 30 series connected units (360 V $\pm$ 40V, 26 Ah) $\approx 10.4$ kWh $\geq Wh_{bat}$
Sizing of PV	Required PV energy capacity ( $Wh_{pv}$ ): $Wh_{day} + Wh_{storage} = 28.125$ kWh Required PV power capacity ( $kW_{pv}$ ): $\frac{Wh_{pv}}{H_{at}} = 5.6$ kW <sub>p</sub> Selected PV module (bifacial type): $V_{mpp} = 40$ V, $I_{mpp} = 9.6$ A, at STC PV array size: 4 $\times$ 4 (4 strings, each string: 4 modules in series) ( $V_{mpp} = 160$ V, $I_{mpp} = 38.4$ A, at STC)

TPC System for stand-alone application.

PV, photovoltaic; TPC, three-port converter.

testing condition). To fulfil the power and energy buffering requirements aligned with the selected load profile, a battery bank of 360 V with a 26 Ah rating is required.

The converter system is capable of efficiently delivering power up to a peak load of 4 kW, but its performance experiences a decline when operating below this threshold. Furthermore, specific constraints related to battery charging and discharging are detailed in the subsequent section for more comprehensive understanding.

## 4.2. Modelling of the proposed bifacial PV/Bat TPC

A DC analysis of the system has been performed, focusing on steady-state conditions and neglecting potential non-idealities. This analysis includes an assessment of volt-seconds and charge balance for all inductors and capacitors within the system, as outlined in Eqs (1)–(3).

$$(v_L)T_s = V_{pv} - V_{bat} (D_{ch}^{eff} - D_{dis}^{eff}) - (1 - D_{pv})V_{dc} = 0 \quad (1)$$

$$(i_{C1})T_s = I_{pv} - I_L = 0 \quad (2)$$

$$(i_{C2})T_s = (1 - D_{pv})I_L - I_{dc} = 0 \quad (3)$$

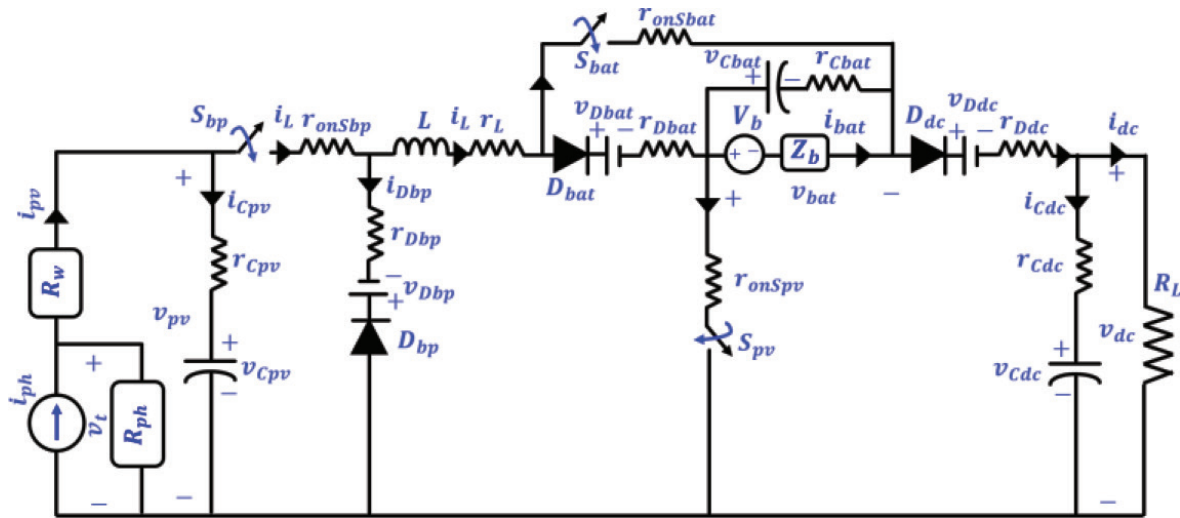


**Figure 5.** Mathematical model of TPC showing all possible non-idealities. TPC, three-port converter.

To explore the dynamic behaviour of the system, a small signal AC analysis has been conducted using a mathematical model of the TPC, as depicted in Figure 5. This analysis provides insights into the system's response to small variations around the steady-state operating points, allowing for the assessment of its dynamic performance and stability. The model presented in this study is designed to account for all possible non-idealities within the system. In contrast, the approach adopted in Villalva et al. (2010) utilised a simpler model that represented the PV array as a voltage source in series with an equivalent resistance. To enhance the model's realism, two key modifications have been introduced in this study:

- Modelling Individual PV Strings:** Instead of treating the PV array as a simple voltage source, this study models individual PV strings as current sources in parallel with an equivalent resistance. This approach applies the source transformation theorem to the model presented in Villalva et al. (2010). By doing so, the model better captures the behaviour of the PV strings and their interaction with the system.
- Accounting for DC Wire Resistance:** The model now includes the unavoidable DC wire resistance ( $R_w$ ) for each PV string, which extends from the rooftop to the converter's input. This resistance is introduced as a series element in the model (as shown in Eq. (4)). This modification is vital because it significantly impacts the actual PV voltage that reaches the converter's input port. By considering this wire resistance, the model becomes more accurate and reflective of real-world conditions.

Furthermore, the model also incorporates the representation of the battery in Eq. (5), considering the use of a lead-acid battery. This modelling approach aligns with the methodology outlined in Moubayed et al. (2008), ensuring a more realistic depiction of the battery's behaviour within the system.

$$i_{pvx} = i_{phx} - \frac{v_{tx}}{R_{phx}} \quad \text{and} \quad v_{pvx} = v_{tx} - i_{pvx} R_w \quad (4)$$

$$i_{bat} = \frac{V_b - v_{bat}}{Z_b} \quad (5)$$

This gives rise to the dynamic equations of TPC as follows:

$$L \frac{di_L}{dt} = v_{Cpv} - (1 - d_{pv}) v_{Cdc} - (d_{ch}^{eff} - d_{dis}^{eff}) v_{bat} - (1 - d_{pv}) v_{Ddc} - (d_{ch}^{eff} + d_{pv}) v_{Dbat} - i_L [r_{onSbp} + r_L + (d_{ch}^{eff} + d_{pv}) r_{Dbat} + d_{pv} r_{onSpv} + (d_{ch}^{eff} + d_{dis}^{eff}) z_b + (1 + d_{dis}^{eff} - d_{pv}) r_{onSbat} + (1 - d_{pv}) r_{Ddc}] \quad (6)$$

$$C_{pv} \frac{dv_{Cpv}}{dt} = i_{pv} - i_L \quad (7)$$

$$C_{dc} \frac{dv_{Cpv}}{dt} = (1 - d_{pv}) i_L - i_{dc} \quad (8)$$

$$C_{bat} \frac{dv_{Cbat}}{dt} = \frac{V_b - v_{bat}}{Z_b} \quad (9)$$

Eqs (6)–(8) can be linearised by introducing small perturbations to the time-varying dynamic variables, as indicated in Eq. (9).

$$j = J + \hat{j}, \text{ where } \hat{j} \ll J \quad (10)$$

where  $j$  represents the dynamic variable averaged over a switching cycle,  $J$  signifies the corresponding steady-state value and  $\hat{j}$  denotes the small signal AC perturbation around its steady-state value. When utilising the state-space linearisation technique, the expressions can be reconfigured to facilitate the analysis of the system's small-signal behaviour and the responses to perturbations around the steady-state conditions are shown in Eqs (11) and (12).

$$[K]_{4 \times 4} \left[ \frac{d\hat{x}}{dt} \right]_{4 \times 1} = [A]_{4 \times 4} [\hat{x}]_{4 \times 1} + [B]_{4 \times 5} [\hat{u}]_{5 \times 1} + [P]_{4 \times 3} [\hat{d}]_{3 \times 1} \quad (11)$$

$$[\hat{y}]_{3 \times 1} = [C]_{3 \times 4} [\hat{x}]_{4 \times 1} + [E]_{3 \times 5} [\hat{u}]_{5 \times 1} + [Q]_{3 \times 3} [\hat{d}]_{3 \times 1} \quad (12)$$

$$[\hat{x}]_{4 \times 1} = \begin{bmatrix} \hat{i}_L \\ \hat{v}_{Cpv} \\ \hat{v}_{Cdc} \\ \hat{v}_{Cbat} \end{bmatrix}_{4 \times 1}, \quad [\hat{u}]_{5 \times 1} = \begin{bmatrix} \hat{i}_{pv} \\ \hat{v}_{bat} \\ \hat{v}_{Dbat} \\ \hat{v}_{Ddc} \\ \hat{i}_{dc} \end{bmatrix}_{5 \times 1} \quad (13)$$

$$[\hat{d}]_{3 \times 1} = \begin{bmatrix} \hat{d}_{pv} \\ \hat{d}_{ch} \\ \hat{d}_{dis} \end{bmatrix}_{3 \times 1}, \quad [\hat{y}]_{3 \times 1} = \begin{bmatrix} \hat{v}_{pv} \\ \hat{v}_{dc} \\ \hat{i}_{bat} \end{bmatrix}_{3 \times 1} \quad (14)$$

In the provided context,  $[\hat{x}]$  represents the perturbed state vector,  $[\hat{u}]$  represents the perturbed input vector and  $[\hat{d}]$  represents the perturbed duty vector. Moreover,  $[A]$ ,  $[B]$  and  $[P]$  encompass the constants of proportionality for the corresponding vectors in Eq. (11),  $[C]$ ,  $[E]$ , and  $[Q]$  contain the same constants in Eq. (12),  $[K]$  represents the values of the state variables and  $[\hat{y}]$  represents the perturbed output vector. The parameter values associated with all the constants of the proportionality matrices are provided in Table 3.

## 5. Implemented Control Schemes

The proposed TPC converter controller, as depicted in Figure 6, employs voltage loops to effectively regulate and control the system. It utilises the existing weather monitoring system (WMS) installed at the bifacial real-time installation site to gather real-time measurements of the front side irradiance ( $G_f$ ), backside irradiance ( $G_b$ ) and temperature ( $T_{inst}$ ). This eliminates the requirement for additional sensors to monitor these environmental parameters, making the system more efficient and cost-effective.

**Table 3.** Parameter values of all the constants of the proportionality matrix.

Matrix	List of parameters
$[K]_{4 \times 4}$	$K_{11} = L, K_{22} = C_{pv}, K_{33} = C_{dc}, K_{44} = C_{bat}$ , and rest all are zero.
$[A]_{4 \times 4}$	$A_{11} = -[r_{onSbp} + r_{onSbat} + R_L + r_{Cpv} + r_{Ddc} + D_{pv}(r_{onSpv} + r_{Dbat} - r_{onSbat} - r_{Ddc}) - (1 - D_{pv})^2 r_{Cdc} + D_{dis}^{eff}(r_{Dbat} + R_b) + D_{ch}^{eff}(r_{onSbat} + R_b)]$ $A_{12} = 1, A_{13} = -(1 - D_{pv}), A_{14} = 0$ $A_{21} = -1$ $A_{31} = (1 - D_{pv})$ , and rest all are zero.
$[B]_{4 \times 5}$	$B_{11} = r_{Cpv}, B_{12} = -(D_{ch}^{eff} - D_{dis}^{eff})$ , $B_{13} = -(D_{ch}^{eff} + D_{pv})$ , $B_{14} = -(1 - D_{pv}), B_{15} = (1 - D_{pv})r_{Cdc}, B_{21} = 1$ , $B_{35} = -1, B_{42} = -1$ and rest are all zero.
$[P]_{4 \times 3}$	$P_{11} = V_{Cdc} + V_{Ddc} - V_{Dbat} - I_L [r_{onSpv} - r_{onSbat} + r_{Dbat} - r_{Ddc} - (1 - D_{pv})r_{Cdc}]$ , $P_{12} = -(R_b I_L + V_{Dbat})$ , $P_{13} = -(r_{onSbat} I_L + R_b I_L)$ , $P_{31} = -I_L$ , rest are all zero.
$[C]_{3 \times 4}$	$C_{11} = -r_{Cpv}, C_{12} = 1, C_{21} = (1 - D_{pv})$ , $C_{23} = 1, C_{21} = (1 - D_{pv})$ , and rest all are zero.
$[E]_{3 \times 5}$	$E_{11} = r_{Cpv}, E_{25} = -r_{Cdc}$ , and rest all are zero.
$[Q]_{4 \times 3}$	$Q_{21} = -I_L r_{Cdc}$ , $Q_{31} = -I_L$ , and rest all are zero.

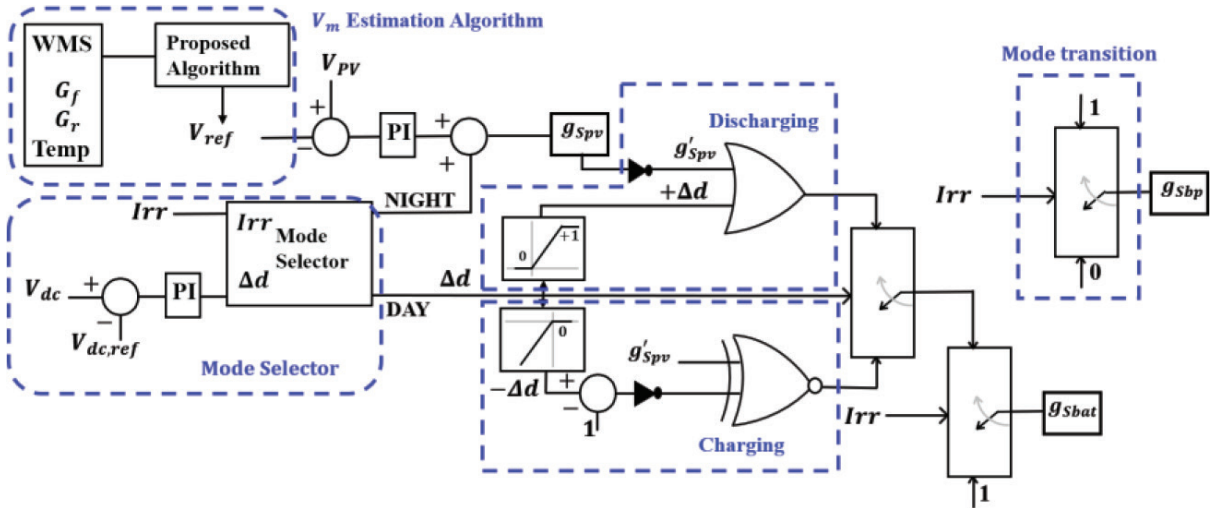


**Figure 6.** Complete control scheme for the proposed DC-DC converter. WMS, weather monitoring system.

The algorithm for estimating the reference voltage ( $V_{ref}$ ) takes advantage of the acquired parameters ( $G_f$ ,  $G_r$ , and  $T_{inst}$ ). Estimating  $V_{ref}$  is crucial for optimising the converter's performance and operation based on the prevailing environmental conditions. The controller requires three voltage sensors for measuring key voltages. The PV voltage is sensed using a voltage sensor denoted as  $V_{pv}$ . This sensed value is then compared with the estimated  $V_{ref}$  to calculate an error, which is further processed by a proportional-integral (PI) controller. The PI controller generates the desired pulse width modulation (PWM) signal for the semiconductor switch  $S_{pv}$ , effectively regulating the PV output voltage. Details of the control are explained in Sahu et al. (2023b).

## 6. Experimental Validation

The proposed TPC topology and control scheme have undergone validation through experimental tests conducted on a 760 W laboratory prototype as shown in Figure 7(a). This prototype is equipped with two bifacial modules connected in series, as shown in Figure 7(b), and a pack of lead-acid battery. The output of the system is connected to a resistive load for simplicity. The DC load voltage for the laboratory prototype is regulated at 110 V in all modes. Parameters used in the experimental study are listed in Table 4.

A DSP control card (TMDSCNCD28379D) platform is responsible for managing the TPC topology, incorporating the presented switching algorithm. This platform facilitates the measurement and recording of current and voltage signals using voltage probes and current probes, while a digital storage oscilloscope (DSO) is employed to observe the system's dynamic behaviour.

The experimental tests encompass a comprehensive series of scenarios, including varying irradiance levels ranging from 100 W/m<sup>2</sup> to 1,000 W/m<sup>2</sup>, both day and night operation and accounting for the charging and discharging

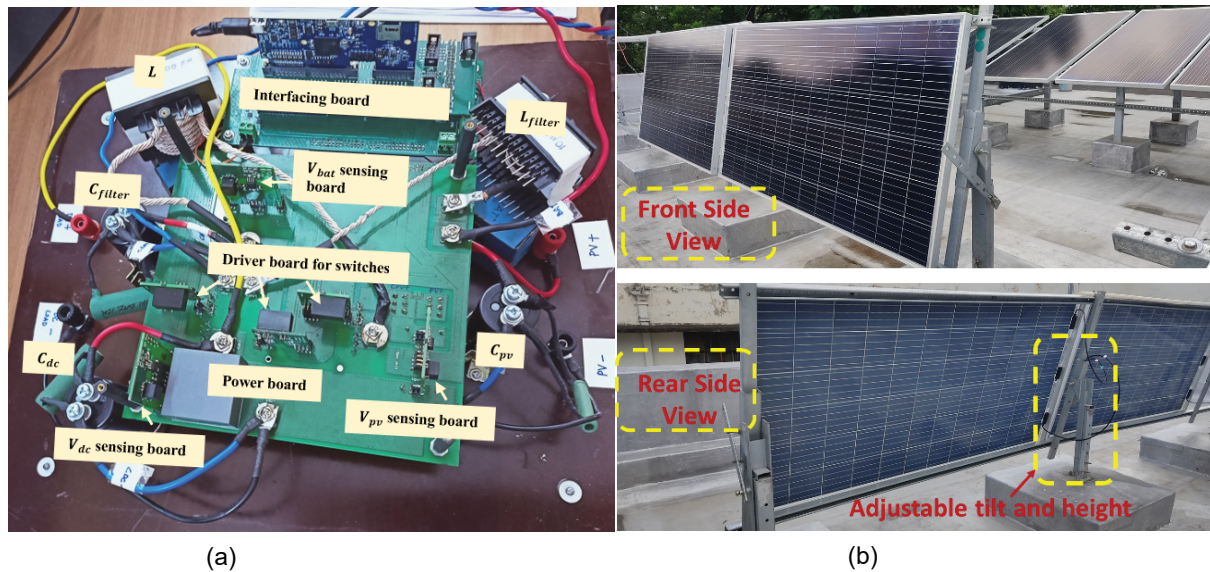


**Figure 7.** (a) Laboratory prototype of the proposed TPC topology and (b) rooftop view of bifacial PV setup. PV, photovoltaic; TPC, three-port converter.

**Table 4.** Parameters used in the experimental study.

Parameters	Values/specifications
PV array	760 W <sub>p</sub> , 48 V, 18 A at STC, bifacial type
Battery	60 V, 26 Ah, lead-acid type
DC link	110 V, Load: 20–180 Ω
Inductors	$L = 100 \mu\text{H}$ , $L_{\text{filter}} = 10 \mu\text{H}$
Capacitors	$C_{pv} = C_{bat} = C_{dc} = 1,000 \mu\text{F}$
Switches	$S_{bp} = S_{pv} = S_{bat} = \text{C3M0045065K}$
Diodes	$D_{bp} = D_{bat} = D_{dc} = \text{E3D30065D}$
Gate driver	ADUM4146BRWZ-RL (ANALOG DEVICES)
Voltage sensors	ACPL-387A-000E (BROADCOM)
Current sensors	CT426-HSN830MR (CROCUS)
Frequency	$F_{sw} = 100 \text{ kHz}$

PV, photovoltaic.

constraints of the battery. Additionally, these tests consider a wide range of load demand, spanning from 0.3 to 1 per unit (pu). These tests are designed to assess the system’s performance under various operating conditions. The results obtained from these experiments are then meticulously compared with the simulation results to ensure consistency and accuracy, thereby validating the effectiveness of the proposed TPC converter topology and control scheme.

The converter’s performance is assessed with three different sequences of modes, as illustrated in Figures 8(a)–(c). These experimental validations substantiate the claims made in Sahu et al. (2023a,b).

### 6.1. Battery charging

During this mode, the battery charging operation takes place (Figure (8a)). Charging occurs when both  $S_{pv}$  and  $S_{bat}$  are turned OFF. The voltage stress across  $S_{pv}$  ( $V_{Spv}$ ) is determined to be 170 V, which is the sum of  $V_{DC}$  and  $V_{bat}$ . Similarly, the voltage stress across  $S_{bat}$  ( $V_{Sbat}$ ) is measured at 60 V, corresponding to  $V_{bat}$ . The average value of the inductor current is recorded at 8.8 A, equivalent to  $I_{pv}$ . This mode effectively showcases the operation of modes 1, 2 and 3, demonstrating how the TPC converter efficiently handles the transition between these modes to regulate the DC link voltage at 110 V and ensure a continuous power supply.

### 6.2. Battery discharging

During this mode, the battery is discharged to supply power to the load (Figure (8b)). Discharging takes place when both  $S_{pv}$  and  $S_{bat}$  are turned ON. In this process, stored energy from the battery is released to maintain the DC link voltage at 110 V and provide power to the load.  $V_{Spv}$  is found to be 170 V, which is the sum of  $V_{DC}$  and  $V_{bat}$ . Similarly,  $V_{Sbat}$  is measured at 60 V, corresponding to  $V_{bat}$ . The average value of the inductor current is recorded at 8.6 A, which is equivalent to  $I_{pv}$ . This mode effectively showcases the operation of modes 1, 2 and 4.

### 6.3. Night mode operation

The night mode operation showcases a scenario where the PV source is not active, such as during nighttime (Figure (8c)). The proposed converter operates effectively when the irradiance level is  $>200 \text{ W/m}^2$ . Below this threshold, the PV system is bypassed due to control limitation, and the battery alone is responsible for regulating the DC link voltage. The converter switches between ON and OFF  $S_{pv}$ , while keeping  $S_{bat}$  continuously ON to ensure a consistent power supply to the load, even in the absence of solar energy.  $V_{Spv}$  is determined to be 170 V, which is the sum of  $V_{DC}$  and  $V_{bat}$ . On the other hand,  $V_{Sbat}$  is 0 V since the switch is continuously turned ON, indicating that the battery is actively supplying power to the load to meet the load demand during the night mode operation. This mode effectively showcases the operation of modes 5 and 6.

These experiments provide a comprehensive understanding of how the TPC converter behaves under various operational conditions, confirming the practical feasibility and effectiveness of the proposed converter topology and control scheme. To provide a more thorough understanding of this topology’s performance, experiments are conducted at different levels of irradiance: low, mid and high. These performance results are shown in Figures 9(a)–(c). In all the waveforms for different levels of irradiance, it is important to note that the  $V_{mpp}$  (maximum power point voltage) was not constant. This variation in  $V_{mpp}$  is attributed to the voltage drop caused by the PV cable running from the installed area to the prototype location. The extent of this voltage drop depends on the irradiance

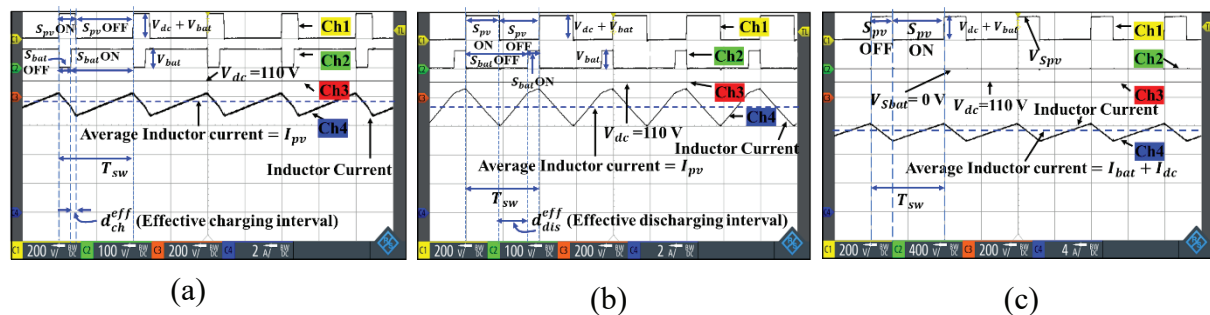


**Figure 8.** System performance during (a) battery charging, (b) battery discharging and (c) nighttime, regulating the DC link voltage at 110 V in each mode.

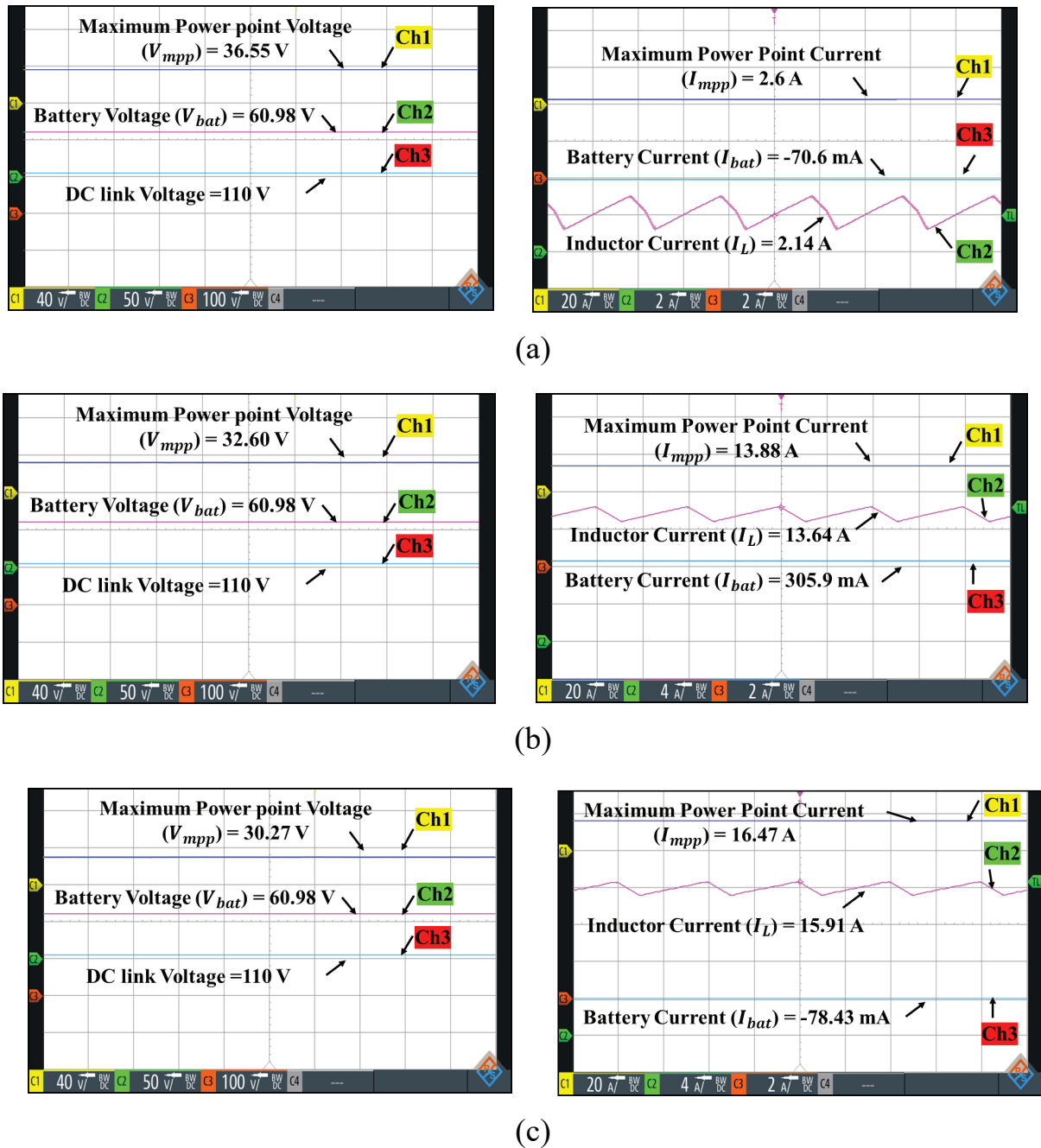


**Figure 9.** System performance during (a) low, (b) mid and (c) high irradiance level.

value and there is an inverse relationship between the two. As irradiance increases, the voltage drop also increases, consequently leading to a decrease in the  $V_{mpp}$ . This phenomenon is a critical factor to consider when designing and optimising systems for different irradiance conditions.

The low-level irradiance corresponds to values  $<300$  W/m<sup>2</sup>, the mid-level falls within the range of 400–700 W/m<sup>2</sup> and the high-level irradiance is defined as values  $>800$  W/m<sup>2</sup>. These experiments allow us to assess how the converter performs under a spectrum of environmental conditions, demonstrating its adaptability and reliability across a range of solar irradiance levels for bifacial PV.

## 7. Performance Stability and Reliability of the Proposed TPC

To ensure performance stability, the charging and discharging constraints of the battery need to be examined. The general expression for  $d_{pv}$  is given as:

$$d_{pv} = \frac{V_{DC} - V_{PV} + (d_{ch} - d_{dis})V_{bat}}{V_{DC}} \quad (15)$$

In the case of charging limitation, the battery charging duty is limited to  $\overline{d_{pv}}$ , with  $d_{ch} \leq \overline{d_{pv}}$ . If  $d_{ch} = 1 - d_{pv}$ ; then Eq. (15) can be modified into Eq. (16);

$$d_{pv} = \frac{V_{DC} - V_{PV} + V_{bat}}{V_{DC} + V_{bat}} \quad (16)$$

Considering system level rating,  $V_{DC} = 700$  V,  $V_{PV} = 160$  V, and  $V_{bat} = 360$  V, then  $d_{pv} = 0.85$ . Thus,  $d_{ch} = 1 - 0.85 = 0.15$  and the battery current,  $I_{bat} = 0.15 \times I_{pv} = 5.76$  A, resulting in a peak charging current of 6 A. If the PV operates at MPPT in a full insolation level, then the peak charging current of the battery is 6 A. The battery power,  $P_{bat} = 360 \times 5.76 = 2,073.6$  W and the PV Power,  $P_{pv} = 160 \times 38.4 = 6,144$  W, leading to a load power,  $P_o$  of 4,070 W. If the load power demand decreases further, the battery needs to charge to regulate the DC link voltage, but due to charging constraints, it cannot charge beyond this limit, causing the PV to shift to OFF MPPT operation.

In the case of discharging limitation, the battery discharging duty is limited to  $d_{pv}$  with  $d_{dis} \leq d_{pv}$ . If  $d_{dis} = d_{pv}$ ; then Eq. (15) can be modified into Eq. (17);

$$d_{pv} = \frac{V_{DC} - V_{PV}}{V_{DC} + V_{bat}} \quad (17)$$

With the same system level rating, we get  $d_{pv}$  as 0.5, hence  $d_{dis}$  is 0.5. In the evening, when solar insolation is considered to be 200 W/m<sup>2</sup>, then the PV current,  $I_{pv}$ , is 8 A (with four panels connected in parallel). Thus, at  $d_{pv} = 0.5$ , the battery current  $I_{bat} = 8 \times 0.5 = 4$  A, resulting in a peak discharging capability of  $360 \times 4 = 1.4$  kW. If the load demand increases beyond 1.4 kW, the battery cannot regulate the DC link voltage due to system limitations. To meet the load demand beyond 1.4 kW at low irradiance, the PV will be bypassed from the circuit ( $S_{bp}$  will be turned off), and only battery mode operation (mode 5 and 6).

To check the stability of the proposed converter, steady-state analysis has been performed. The resulting control-to-PV voltage transfer function is obtained as Eq. (18), by substituting the respective parametric values from the simulation.

$$G(s) = \frac{\hat{v}_{pv}(s)}{\hat{d}_{pv}(s)} = \frac{6,000s^2 - 1.844e^{-8}s + 1.602e^{-20}}{s^3 + 691.5s^2 + 1.005e^8s - 0.0001582} \quad (18)$$

The location of poles is  $(-0.0346 \pm i1.0021) \times 10^4$  and 0, and the location of zeros is  $0.2306 \times 10^{-11}$  and  $0.0768 \times 10^{-11}$ . The frequency response of the uncompensated boost converter, shown in Figure 10(a), indicates a phase margin (PM) of  $-96.6^\circ$  at a 12 kHz gain cross-over frequency (GCF) and a gain margin (GM) of 323 dB at a 0 kHz phase cross-over frequency (PCF). The negative value of PM signifies that the uncompensated proposed converter in closed loop with unity feedback is unstable. Additionally, the system has two zeros at low frequency, which can be identified by the transfer function (Eq. (18)). This necessitates the design of a compensator in such a way that the resulting compensated system should give a stable and well-regulated PV voltage.

Hence, in the compensated system as shown in Figure 10(b), two poles at the origin are added to nullify the initial slope occurring due to the presence of two zeros at low frequency. The compensated system has a positive PM ( $89.8^\circ$ ) with a reasonable bandwidth and a settling time of 0.03 s as shown in Figure 11. Similarly, the control-to-output voltage transfer function has been derived to ensure system stability and performance.

To enhance reliability, a fault analysis of the proposed converter has been conducted to enhance its reliability, identifying potential fault scenarios and providing mitigation strategies to ensure system stability and robustness.

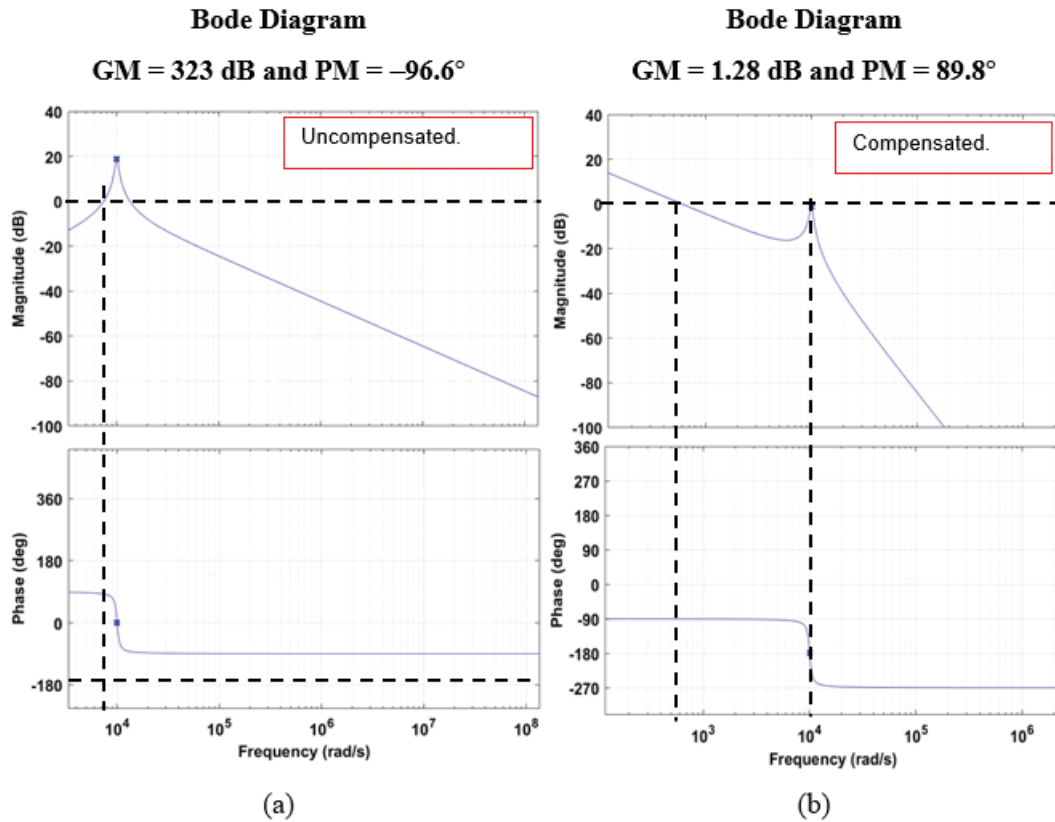


**Figure 10.** Frequency response of (a) uncompensated and (b) compensated proposed converter. GM, gain margin; PM, phase margin.

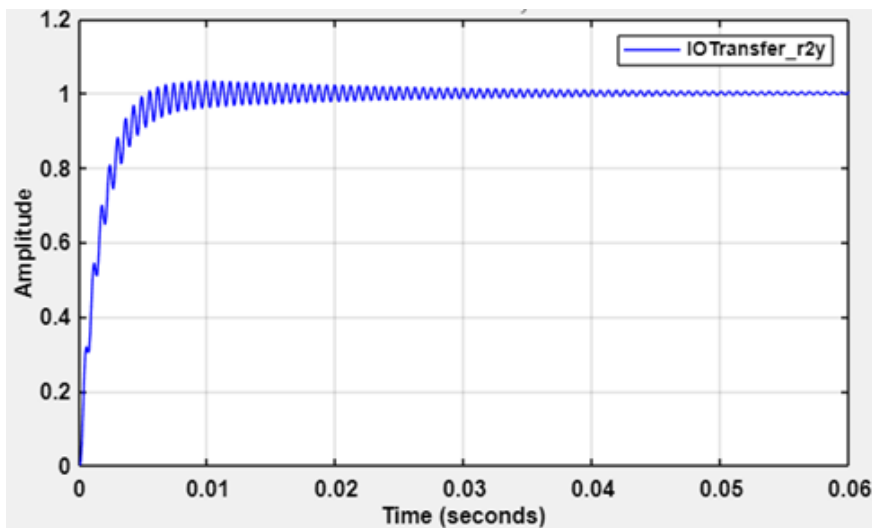


**Figure 11.** Step response of the proposed converter.

The detailed analysis focuses on examining open and short circuit faults in the switches  $S_{bp}$ ,  $S_{pv}$  and  $S_{bat}$ . In the case of a fault in  $S_{bp}$ , whether it is an open or short circuit, the circuit will continue to function with the battery responsible for regulating the DC voltage to the desired value. However, if there is a fault in  $S_{bat}$ , the consequences differ based on the nature of the fault. An open-circuited  $S_{bat}$  results in the battery always charging, causing the circuit to function

but preventing the DC link voltage from being regulated at the desired value. Conversely, a short-circuited  $S_{bat}$  leads to continuous battery discharge. If the PV power is sufficient, the PV will attempt to regulate the DC link voltage by entering the OFF MPPT mode; otherwise, the battery may be damaged. Finally, a fault in  $S_{pv}$ , the main switch of the converter, renders the circuit non-functional.

Therefore, while the topology depends critically on the main switch, the converter can still operate with faults in the other two switches, although it will not meet the desired functionality.

## 8. Comparison with the Existing Tri-Port Converters

A qualitative comparison of the proposed Bifacial PV/Bat TPC with the existing state-of-the-art TPC topologies in terms of various aspects is summarised in Table 5. The topologies in Li et al. (2011), Mohammadi et al. (2022) and Wang and Li (2012) are the closest match for this application. In terms of components, these topologies typically utilise 6–10 switches and diodes, along with up to 6 inductors and 6 capacitors. In contrast, the PV/Bat TPC falls in middle ground, employing 3 switches, 3 diodes and 2 inductors, offering the added advantage of only 1–3 conducting elements being active at any given time, thus minimising power losses. This is further supported by the loss analysis conducted in the preceding section, demonstrating a sound efficiency of 94.15%.

This thorough comparison confirms the superiority of the proposed PV/Bat TPC, meeting all desired objectives with a reasonable number of components. Furthermore, it presents the option for bifacial PV for day and night operation, targeting stand-alone applications.

## 9. Loss Analysis and Efficiency Calculation

The total loss  $L_{tot}$  of the converter is the sum of three components: total conduction losses  $L_{con}^{tot}$ , total switching losses  $L_{sw}^{tot}$ , and inductor loss  $L_{ind}^{tot}$ , as discussed in detail in Karpana et al. (2024). Table 6 provides the expressions for RMS (root mean square) and average currents for switches and diodes, which are functions of  $I_L$  (approximated with small ripple). It is essential to highlight that the loss analysis is conducted based on the targeted system ratings outlined in Table 2.

$$L_{tot} = L_{con}^{tot} + L_{sw}^{tot} + L_{ind}^{tot} \tag{19}$$

**Table 5.** Comparison of the proposed PV/Bat TPC with the existing non-isolated TPC topologies.

Grounds of comparison	Li et al. (2011)	Mohammadi et al. (2022)	Wang et al. (2012)	PV/Bat TPC
Switches	4	3	6	3
Diodes	2	3	4	3
Inductors	5	3	4	2
Capacitors	2	2	6	2
Switches/diodes conduct at any instant	2–4	1–4	3–4	1–3
PV with energy storage	✓	✓	✓	✓
Validation of topology for bifacial PV	–	–		✓

PV, photovoltaic; PV/Bat TPC, PV/Bat Tri-port DC-DC Converter; TPC, three-port converter.

**Table 6.** RMS and average current ratings.

Switches	RMS current	Diodes
$S_{bp}$	$I_L$	$Diode_{bp}$
$S_{pv}$	$I_L \sqrt{d_{pv}}$	$Diode_{bat}$
$S_{bat}$	$I_L \sqrt{d_{bat}^{ch/dis}}$	$Diode_{dc}$

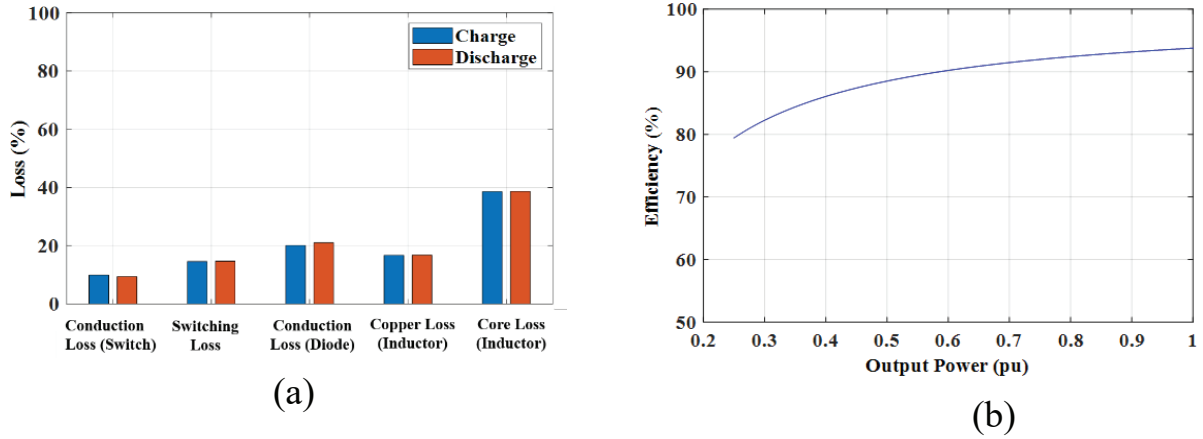


**Figure 12.** (a) Loss breakdown of the TPC and (b) Efficiency curves with load variation from 25% of the load to full load. TPC, three-port converter.

A generalised expression for  $d_{pv}$  irrespective of the modes of the operation can be given by,

$$d_{pv} = \frac{V_{dc} - V_{pv} + V_{Ddc} + d_{ch}^{eff} V_{Dbat} + (d_{ch}^{eff} - d_{dis}^{eff}) V_{bat} + I_L [r_L + r_{onSpv} + d_{ch}^{eff} r_{Dbat} + (1 + d_{dis}^{eff}) r_{onSbat} + (d_{ch}^{eff} - d_{dis}^{eff}) Z_b + r_{Ddc}]}{V_{dc} + V_{Ddc} - V_{Dbat} - I_L [r_{Dbat} - r_{onSbat} - r_{Ddc} + r_{onSpv}]} \quad (20)$$

The analysis of TPC converter performance, including both loss and efficiency, is illustrated in Figure 12(a). This assessment considers the PV system's specifications outlined in Table 2 and aligns with the capabilities of the converter detailed above. It is crucial to emphasise that the PV operates under STC, and the battery voltage is set at 360 V. The SiC MOSFET parameters ( $r_{on}$ ) and Schottky diode parameters ( $V_d$ ) are defined as 21 m $\Omega$  and 1.5 V, respectively.

The inductor's resistance ( $r_L$ ) is determined to be 30 m $\Omega$ , with the associated core loss attributed to six N97: E/70/33/32 ferrite cores. For this specific core arrangement, the datasheet specifies a core loss of 17.2 W per core at a switching frequency ( $F_{sw}$ ) of 100 kHz and a peak flux density of 0.2 T.

As illustrated in Figure 12(b), the system achieves an efficiency of nearly 94.15% at rated load. However, efficiency gradually diminishes when transitioning from the rated load to half load or even 25% of the load.

## 10. Conclusion

This paper presents a comprehensive and concise approach to hybridising small-scale bifacial PV systems with batteries for stand-alone applications. It addresses the challenges of self-shading in bifacial PV systems, thereby improving the efficient utilisation of energy from PV sources for stand-alone power supply. The proposed tri-port converter, achieved by integrating two additional switches and diodes into a standard boost converter, plays a crucial role in efficiently harnessing energy from both bifacial PV and batteries.

Modelling and hardware validation of the proposed tri-port converter have been conducted to enable controlled DC link operation during both day and night times. The experimental results validated the analysis of the operating principle. The control techniques facilitate seamless transitions between different operating modes, ensuring a consistent power supply to the load, regardless of whether the PV source is actively generating power or not. Furthermore, the 94.15% peak efficiency is achieved at rated load.

In summary, the proposed tri-port converter offers a viable solution for stand-alone applications with bifacial PV systems. It effectively addresses self-shading issues and ensures efficient energy transfer from the PV system to both the load and the battery. This technology represents a promising step towards achieving sustainable and reliable power supply, at all conditions.

## Acknowledgement

This work was financially supported by the Royal Academy of Engineering under the Engineering for Development Research Fellowship Scheme under Grant RF/201819/18/86, Government of UK.

## References

- Batzelis, E. I. (2017). Simple PV Performance Equations Theoretically Well Founded on the Single-Diode Model. *IEEE Journal of Photovoltaics*, 7(5), pp. 1400–1409. doi: 10.1109/JPHOTOV.2017.2711431
- Bhattacharjee, A. K., Kutkut, N. and Batarseh, I. (2018). Review of Multiport Converters for Solar and Energy Storage Integration. *IEEE Transactions on Power Electronics*, 34(2), pp. 1431–1445. doi: 10.1109/TPEL.2018.2830788
- Bird, L., Milligan, M. and Lew, D. (2013). *Integrating Variable Renewable Energy: Challenges and Solutions* (No. NREL/TP-6A20-60451). Golden, CO, US: National Renewable Energy Lab (NREL).
- de Melo, K. B., da Silva, M. K., de Souza Silva, J. L., Costa, T. S. and Villalva, M. G. (2022). Study of Energy Improvement with the Insertion of Bifacial Modules and Solar Trackers in Photovoltaic Installations in Brazil. *Renewable Energy Focus*, 41, pp. 179–187. doi: 10.1016/j.ref.2022.02.005
- IEA, “Renewable Electricity Growth Is Accelerating Faster than Ever Worldwide, Supporting the Emergence of the New Global Energy Economy,” News, pp. p–1, 2021. <https://www.iea.org/news/renewable-electricity-growth-is-accelerating-faster-than-ever-worldwide-supporting-the-emergence-of-the-new-global-energy-economy>
- Karpana, S., Batzelis, E., Kampitsis, G., Maiti, S. and Chakraborty, C. (2024). A Soft-Switched Multi-Port Converter for PV/Supercapacitors Hybrid Systems Enabling Frequency Response Services. *IEEE Transactions on Industry Applications*, PP (99), pp. 1–15. doi: 10.1109/TIA.2024.3351628
- Li, Q. and Wolfs, P. (2008). A Review of the Single Phase Photovoltaic Module Integrated Converter Topologies with Three Different DC Link Configurations. *IEEE Transactions on Power Electronics*, 23(3), pp. 1320–1333. doi: 10.1109/TPEL.2008.920883
- Li, W., Xiao, J., Zhao, Y. and He, X. (2011). PWM Plus Phase Angle Shift (PPAS) Control Scheme for Combined Multiport DC/DC Converters. *IEEE Transactions on Power Electronics*, 27(3), pp. 1479–1489. doi: 10.1109/TPEL.2011.2163826
- Manuel, N. L. and İnanç, N. (2022). Sliding Mode Control-Based MPPT and Output Voltage Regulation of a Stand-alone PV System. *Power Electronics and Drives*, 7(1), pp. 159–173. doi: 10.2478/pead-2022-0012
- Mohammadi, K., Abbasi, V. and Tanha, K. M. (2022). Three-Port DC-DC Converter for Stand-Alone PV/Battery Systems with Four Operation Modes. *International Journal of Circuit Theory and Applications*, 50(7), pp. 2584–2614. doi: 10.1002/cta.3273
- Moubayed, N., Kouta, J., El-Ali, A., Dernayka, H. and Outbib, R. (2008, May). Parameter identification of the lead-acid battery model. In: *2008 33rd IEEE Photovoltaic Specialists Conference*. San Diego, CA, USA: IEEE, pp. 1–6.
- N-type PERC Bifacial PV Module*. (2022, October). Adani. [Online]. Available: <https://5.imimg.com/data5/SM/PR/AA/SELLER-12708464/adani-solar-panel.pdf>
- Perera, H. M. R. and Wen, H. (2019, August). Power generation and performance analysis of Bifacial vs Mono-facial 10KW Photovoltaic power station. In: *2019 18th International Conference on Optical Communications and Networks (ICOON)*. Huangshan, China: IEEE, pp. 1–3.
- Phimu, K., Singh, K. J. and Dhar, R. S. (2021, October). Efficient optimization technique for analysing the performance of bifacial solar cells using fuzzy logic. In: *International Conference on Computational Techniques and Applications*. Singapore: Springer Nature Singapore, pp. 263–272.
- Raina, G., Mathur, S. and Sinha, S. (2022). Behavior of Bifacial and Monofacial Photovoltaic Modules Under Partial Shading Scenarios. *International Journal of Energy Research*, 46(9), pp. 12837–12853. doi: 10.1002/er.8057
- Sahu, P. K., Karpana, S., Chakraborty, C. and Roy, J. N. (2023b, December). A bifacial PV/battery three port hybrid system for stand-alone applications. In: *2023*

- IEEE 2nd Industrial Electronics Society Annual On-Line Conference (ONCON)*. SC, USA: IEEE, pp. 1–6.
- Sahu, P. K., Roy, J. N. and Chakraborty, C. (2023a). Performance Assessment of a Bifacial PV System Using a New Energy Estimation Model. *Solar Energy*, 262, p. 111818. doi: 10.1016/j.solener.2023.111818
- Selvaraj, J. and Rahim, N. A. (2008). Multilevel Inverter for Grid-Connected PV System Employing Digital PI Controller. *IEEE Transactions on Industrial Electronics*, 56(1), pp. 149–158. doi: 10.1109/TIE.2008.928116
- Siddiqui, N., Verma, A. and Shrivastava, D. (2023, March). Fuzzy logic-based MPPT control for bifacial photovoltaic module. In: *2023 Second International Conference on Electronics and Renewable Systems (ICEARS)*. Tuticorin, India: IEEE, pp. 1–6.
- Siddiqui, N., Verma, A. and Srivastava, D. (2022, December). Perturb and observe algorithm for MPPT of bifacial photovoltaic module. In: *2022 IEEE International Power and Renewable Energy Conference (IPRECON)*. Kollam, India: IEEE, pp. 1–6.
- Villalva, M. G., De Siqueira, T. G. and Ruppert, E. (2010). Voltage Regulation of Photovoltaic Arrays: Small-Signal Analysis and Control Design. *IET Power Electronics*, 3(6), pp. 869–880. doi: 10.1049/iet-pel.2008.0344
- Vračar, D. and Pejović, P. (2022). Active-Clamped Flyback DC-DC Converter in an 800V Application: Design Notes and Control Aspects. *Journal of Electrical Engineering*, 73(4), pp. 237–247. doi: 10.2478/jee-2022-0032
- Wang, Z. and Li, H. (2012). An Integrated Three-Port Bidirectional DC–DC Converter for PV Application on a DC Distribution System. *IEEE Transactions on Power Electronics*, 28(10), pp. 4612–4624. doi: 10.1109/TPEL.2012.2236580
- Zhen, Y., Zuyu, W., Ninghui, Z., Ligen, Y. and Jing Yu, C. (2021). MATLAB Modelling of Double Sided Photovoltaic Cell Module. *Power Electronics and Drives*, 6(1), pp. 12–25. doi: 10.2478/pead-2021-0002